frontiers | Frontiers in Materials

ORIGINAL RESEARCH
published: 19 May 2022
doi: 10.3389/fmats.2022.874899

Corrosion Inhibition and Adsorption Process of 3-Amino-5-Mercapto-1,2,4-Triazole on Aluminium Alloy: Experimental and Theoretical Studies

Xin Guo[1,2,3], *Jinke Wang*[1,2], *Luyao Huang*[4], *Yajie Wang*[1,2], *Li Ma*[3], *Dawei Zhang*[1,2]* and *Lingwei Ma*[1,2,3]*

[1]Beijing Advanced Innovation Center for Materials Genome Engineering, Institute for Advanced Materials and Technology, University of Science and Technology Beijing, Beijing, China, [2]National Materials Corrosion and Protection Data Center, University of Science and Technology Beijing, Beijing, China, [3]State Key Laboratory for Marine Corrosion and Protection, Luoyang Ship Material Research Institute (LSMRI), Qingdao, China, [4]State Key Laboratory of Advanced Power Transmission Technology, Global Energy Interconnection Research Institute Co., Ltd., Beijing, China

The corrosion inhibition effect of 3-amino-5-mercapto-1,2,4-triazole (AMT) on AA2024 aluminium alloy in 3.5 wt.% NaCl solution was investigated, and the corrosion inhibition mechanism was revealed. The influence of AMT concentration on the corrosion inhibition performance was evaluated by potentiodynamic polarization curve and electrochemical impedance spectroscopy (EIS). Surface analysis and surface-enhanced Raman scattering (SERS) spectra were used to study the adsorption process and corrosion inhibition mechanism of AMT on the alloy surface. Polarization curve and EIS results showed that when the AMT concentration was 1.5 g/L, the corrosion current density (i_{corr}) was the lowest and the resistance of adsorption film (R_f) was the largest, illustrating the highest corrosion inhibition efficiency. Moreover, the adsorption kinetics process of AMT was revealed by SERS measurement, and a positive correlation between the SERS intensity and R_f values of AMT after different immersion time was achieved. It indicated that the efficient adsorption of corrosion inhibitors significantly enhanced the corrosion inhibition performance. Density functional theory (DFT) and molecular dynamics simulations were used to give further insight into the adsorption and inhibition mechanism of AMT on the aluminium alloy surface.

Keywords: aluminium alloy, 3-amino-5-mercapto-1,2,4-triazole, corrosion inhibition, surface-enhanced Raman scattering, adsorption process

OPEN ACCESS

Edited by:
Roger Charles Newman,
University of Toronto, Canada

Reviewed by:
Saviour A. Umoren,
King Fahd University of Petroleum and Minerals, Saudi Arabia
Renhui Zhang,
East China Jiaotong University, China

***Correspondence:**
Dawei Zhang
dzhang@ustb.edu.cn
Lingwei Ma
mlw1215@ustb.edu.cn

Specialty section:
This article was submitted to Environmental Degradation of Materials, a section of the journal Frontiers in Materials

Received: *13 February 2022*
Accepted: *31 March 2022*
Published: *19 May 2022*

Citation:
Guo X, Wang J, Huang L, Wang Y, Ma L, Zhang D and Ma L (2022) Corrosion Inhibition and Adsorption Process of 3-Amino-5-Mercapto-1,2,4-Triazole on Aluminium Alloy: Experimental and Theoretical Studies. Front. Mater. 9:874899. doi: 10.3389/fmats.2022.874899

INTRODUCTION

Because of the high strength, low density (about 2.7 g/cm^3), good electrical and thermal conductivity, as well as easy mechanical processing, aluminium alloys have great application prospects and irreplaceable importance in the fields of automotive manufacturing, light construction materials, aerospace, shipping, and military hardware. One of the most widely used aluminium alloys is AA2024 aluminium alloy, which has high specific strength and high fatigue strength (Marcelin and Pébère, 2015; Wang et al., 2017). Although the presence of alloying elements such as copper and magnesium enhances the mechanical properties of the aluminium matrix, it also reduces the corrosion resistance due to the presence of intermetallic particles (IMPs) with segregation at grain

boundaries (Recloux et al., 2018). The presence of IMPs results in the high corrosion sensitivity of the alloy due to the potential difference between the IMPs and the alloy matrix (Parvizi et al., 2018). In particular, the Al_2CuMg particles (also called S-phase) with more negative potential and higher electrochemical activity will be the initial sites of localized corrosion on the aluminium alloy (Hashimoto et al., 2016).

The utilization of organic/inorganic inhibitors is considered as one of the most useful means to prevent metals against corrosion degradation (Wang et al., 2018; Al Zoubi and Ko, 2019). The corrosion efficiency of these inhibitors depends on their adsorption ability on the metal surface *via* active sites, such as π-bonds, heteroatoms (N, S, and O), and polar functional groups (Qiang et al., 2016). Thus, the adsorption films can be formed on metals through covalent bonding (chemisorption) and/or electrostatic interaction (physical adsorption), which can protect metals from corrosive attack (Dutta et al., 2017; Hao et al., 2017). Recently, novel corrosion inhibitors with low toxicity, promising inhibitory efficacy and cost effectiveness have been the subject of current and long-term research focus. Among many nitrogenous compounds used as inhibitors, triazoles, tetrazoles, imidazoles, thiadiazoles and their derivatives are considered as environmental friendly chemicals that are harmless to the human health and the environment (Abdallah, 2004; El-Naggar, 2007; Obot et al., 2009).

3-amino-5-mercapto-1,2,4-triazole (AMT), a 5-membered heterocyclic compound containing a thiol group and an amino group, has been recognized as a good corrosion inhibitor for copper and copper alloys because of its strong adsorption ability on metal surfaces (Balbo et al., 2012). Yu et al. (2010) investigated the corrosion inhibition effect of AMT against copper corrosion in 3.5 wt.% NaCl solution. The inhibition efficiency (IE) increased with the AMT concentration, and the IE% maintained about 94% with an AMT concentration of 5×10^{-3} mol/L. The adsorption of AMT obeyed the Langmuir adsorption isotherm on copper surface, and the adsorption type was chemical adsorption. Sherif and Park (2006) studied the corrosion behavior of unalloyed copper in 0.5 M HCl with and without AMT inhibitors. The weight loss and corrosion rate of copper decreased with the increase of AMT concentration. The strong adsorption of AMT on the copper surface was confirmed by Raman spectra, hence preventing the formation of cuprous chloride and oxychloride complex. However, to the best of our knowledge, the corrosion inhibition effect of AMT on aluminium alloy has not been investigated yet. The fundamental mechanism of the proposed inhibiting interactions and the formation of corrosion protective layer for aluminium alloy are not well-understood, which are pivotal in evaluating the inhibitory performance of AMT molecules.

In this study, the adsorption performance and corrosion inhibition mechanism of AMT on AA2024 aluminium alloy in 3.5 wt.% NaCl solution are presented. The corrosion inhibition effect of AMT was evaluated by potentiodynamic polarization curve, electrochemical impedance spectroscopy (EIS) and surface observation techniques. Surface-enhanced Raman scattering (SERS) technique was applied to obtain the enhanced Raman spectra of corrosion inhibitors adsorbed on the surface of aluminium alloy after different immersion time. Furthermore, the corresponding adsorption and inhibition mechanism at the molecular level are proposed by density functional theory (DFT) and molecular dynamics simulations. This work provides new insights into the inhibition mechanism of organic inhibitors and offers practical guidance for the application of AMT as an effective inhibitor in industrial applications.

MATERIAL AND METHODS

Materials

AA20204 alloy ($4.0 \times 3.0 \times 0.1\ cm^3$) consists the following compositions: Cu 3.94 wt.%, Mg 1.46 wt.%, Mn 0.85 wt.%, Fe 0.45 wt.%, Zn 0.10 wt.%, Cr 0.05 wt.%, Si 0.05 wt.% and Al balance. The AA2024 alloy was successively polished by 400, 800, 1,500 and 2,000 grit sandpapers, and was washed thoroughly by ethanol before use. AMT and NaCl were purchased from Aladdin and used as received.

Electrochemical Tests

EIS and potentiodynamic polarization curves were performed by CHI 660E workstation based on a three-electrode system at room temperature. AA2024 aluminium alloy, platinum foil, and saturated calomel electrode were employed as the working electrode (WE), the counter electrode, and the reference electrode (RE), respectively. Before each measurement, the AA2024 alloy was dipped into 3.5 wt.% NaCl solution at an open circuit potential (OCP) for half an hour. Thereafter, EIS tests were recorded in the frequency range from 0.01 Hz to 100 kHz with a sinusoidal perturbation of 10 mV potential amplitude. Potentiodynamic polarization curves were obtained by scanning within ±250 mV potential range at 0.1666 mV s^{-1} versus OCP. Three parallel tests were performed under the same condition. To calculate the inhibition efficiency from polarization measurements, **Equation 1** was used:

$$IE(\%) = \frac{i_{corr,0} - i_{corr,i}}{i_{corr,0}} \times 100 \quad (1)$$

where $i_{corr,0}$ and $i_{corr,i}$ are the corrosion current densities in the absence and presence of corrosion inhibitors, respectively.

Surface Analysis

The corrosion morphology and chemical composition of the alloy surfaces after immersion in 3.5 wt.% NaCl solution for 72 h without and with AMT inhibitor were characterized by scanning electron microscopy (SEM, Merlin, Zeiss) and energy dispersive X-ray spectroscopy (EDX). The surface roughness of AA2024 surfaces was tested by confocal laser scanning microscopy (CLSM, VK-X, Keyence). Water contact angle (WCA) was calculated by a contact angle meter (Dataphysics OCA25) with a DI water drop volume of 5 μL at room temperature. A high-resolution camera was used to capture the static water images, and WCAs were calculated using the image processing software. The chemical

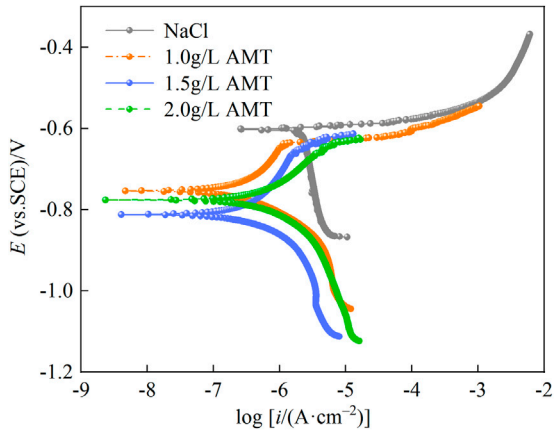

FIGURE 1 | Polarization curves of aluminium alloy after 6 h of immersion in 3.5 wt.% NaCl solution without and with various concentrations of AMT (1.0, 1.5, 2.0 g/L).

compositions of the uninhibited and inhibitor adsorbed alloy surfaces were analyzed by X-ray photoelectron spectroscopy (XPS, K-Alpha, Thermo Scientific).

Surface-Enhanced Raman Scattering Detection

To characterize the adsorption of AMT on the AA2024 alloy surface, SERS spectra were measured by a Raman spectrometer (i-Raman Plus, B&W TEK Inc.) equipped with a 785 nm laser and at a laser power of 150 mW (Wang et al., 2021). A SERS active tape was pasted onto the alloy surface before SERS detection. The diameter of the laser spot was ~80 μm, and the acquisition time was set to be 10 s for each detection spot. Five spectra were recorded on each substrate to ensure reproducibility.

Density Functional Theory Study

To investigate the electronic structure of AMT inhibitor, the quantum calculation method was adopted by DFT at the level B3LYP/6-311G++ base set (d) using the Gaussian 09 and GaussView 5.0.8 software (Zhang et al., 2020). Besides, the Fukui indices can be used to reflect the local reactivity of molecules. They determine the electron density in response to electrophilic or nucleophilic attack. The Fukui indices calculated from Mulliken's population value are as follows (El-Hajjaji et al., 2020), where $P_k(N+1)$, $P_k(N)$ and $P_k(N-1)$ are the charge values of k atoms to cations, neutral and anions, respectively.

For nuclearophilic attack

$$fk^{+} = P_k(N+1) - P_k(N) \tag{2}$$

For electrophilic attack

$$fk^{-} = P_k(N) - P_k(N-1) \tag{3}$$

Moreover, it is necessary to study the adsorption mode and binding strength of inhibitor on metal surface. The interaction nature between the inhibitor molecule and aluminium was performed using molecular mechanics method as implemented in Forcite module of Material studio 8.0 software. A simulation box of $34.18 \times 34.18 \times 68.86$ Å^3 dimension containing six layers of Al (111), one inhibitor molecule, 500 H_2O molecules, 5 Cl^-, 5 Na^+ and 40 Å vacuum layer was established. The periodic boundary condition and COMPASS force field were used in this system. A fine quality simulation was accomplished with 500 ps simulation time and 1 fs time step using NVT canonical ensemble.

RESULTS AND DISCUSSION

Potentiodynamic Polarization

The corrosion inhibition effect of AMT on AA2024 substrate was first assessed by potentiodynamic polarization. **Figure 1** shows the polarization curves of aluminium alloy after 6 h of immersion in 3.5 wt.% NaCl solution without and with various concentrations of AMT (1.0, 1.5, 2.0 g/L). It can be seen that the application of inhibitors made the corrosion potential (E_{corr}) shift towards the negative potential and significantly decreased the corrosion current density (i_{corr}). The cathodic current density decreased evidently, indicating that AMT mainly acted as a cathode-type inhibitor to restrict the oxygen diffusion process (Shen et al., 2013). In the anodic branch, the polarization curve of the sample immersed in blank NaCl solution showed immediate pitting and the E_{corr} was around −0.60 V. With the addition of AMT, a passivation behavior of the alloy was observed, which was associated with the formation of a protective film via the adsorption of inhibitors. The fitted E_{corr} and i_{corr} parameters along with the inhibition efficiency are listed in **Table 1**. As can be seen, the i_{corr} values decreased apparently with the addition of inhibitors. The lowest i_{corr} value was observed for aluminium alloy in the presence of 1.5 g/L AMT (0.239 μA/cm^2), which was reduced by one order of magnitude compared with that of the blank alloy sample (2.397 μA/cm^2). The inhibition efficiencies were calculated to be 87.6% for 1.0 g/L AMT, 90.0% for 1.5 g/L AMT, and 82.6% for 2.0 g/L AMT, respectively, demonstrating superior suppression of the corrosion process in saline solutions.

Electrochemical Impedance Spectroscopy

The corrosion inhibition effect of AMT was further examined by EIS measurement. **Figure 2** shows the Nyquist diagrams and Bode plots of AA2024 aluminium alloy in 3.5 wt.% NaCl solution containing different concentrations of AMT inhibitors. The measured impedance implies the capacitive and resistive properties of the inhibitor film and is related to the corrosion kinetic of the metal in aggressive media. In the Nyquist diagrams, the capacitive loops of the blank alloy sample were relatively small, which decreased gradually with the increase of immersion time. After the addition of AMT, the diameter of capacitive loops increased significantly, and enlarged with the prolonging of immersion time. When the AMT concentration was 1.5 g/L, the capacitive loops reached the maximum. The impedance modulus plots illustrated similar trend, i.e., the impedance magnitude of aluminium alloy increased considerably after the addition of AMT, and reached the highest values when the AMT concentration was 1.5 g/L. In general, the low frequency

TABLE 1 | Polarization curve fitting data of AA2024 aluminium alloy in 3.5 wt.% NaCl solution containing different concentrations of AMT.

AMT concentration	E_{corr} (V)	i_{corr} (×10^{-6}A/cm^2)	-β_c (mV dec^{-1})	β_a (mV dec^{-1})	*IE* (%)
0	−0.601	2.397	1,092.8	15.5	—
1.0 g/L	−0.753	0.298	96.6	171.5	87.6%
1.5 g/L	−0.812	0.239	98.2	176.8	90.0%
2.0 g/L	−0.776	0.418	97.8	110.1	82.6%

impedance modulus $|Z|_{0.01Hz}$ is used as a semi-quantitative measure of the corrosion resistance property. After 72 h, the exposure to AMT solution led to the increase of $|Z|_{0.01Hz}$ value by more than 50 times compared to that of the blank alloy. Regarding to the phase angle plots, the blank AA2024 alloy possessed two time constants, the one in the low frequency (10^{-2}–10^{0} Hz) represented the charge transfer process, and the one in the mid frequency (10^{0}–10^{3} Hz) was assigned to the formation of metal oxide layer on the substrate (Liu et al., 2016; Ma et al., 2021). In contrast, with the addition of AMT inhibitors, the corrosion electrochemical process in the low-frequency region was greatly suppressed (Liao et al., 2017), and the broader time constant in the middle-to-high frequency indicated that the corrosion inhibitor was effectively adsorbed on the surface of aluminium alloy to form a robust protection layer (Zeng et al., 2021).

To verify the EIS interpretation, the electric equivalent circuits (EECs) in **Figure 3** are selected to fit the data in **Figure 2**, (Coelho et al., 2018). The EEC without inductance includes a solution resistance (R_s) in series with a constant phase element (CPE_f) in parallel with a film resistance (R_f) in series with another constant phase element (CPE_{dl}) in parallel with a charge transfer resistance (R_{ct}). The inductive loop (L) occurred due to the alloy dissolution during the adsorption process or due to the presence of the by-products on the electrode surface. Without AMT, R_f and CPE_f represent the resistance and the constant phase element of the native oxide layer (Fekry et al., 2014). For the inhibited substrates, R_f and CPE_f are assigned to the resistance and constant phase element of the inhibitor film (Yan et al., 2020; Zhu et al., 2021; Cao et al., 2022). CPE_{dl} corresponds to the double layer capacitance. The fitted EIS parameters are presented in **Table 2** and **Figure 4**. It is shown that the addition of AMT increased the $\underline{R}_{ct}$ and R_f values and the inhibition performance was promoted with increasing the AMT concentration. At the same time, the values of CPE_f and CPE_{dl} tended to decrease as the increase of AMT concentration due to the increase of AMT layer thickness and/or the local dielectric constant. It can be concluded that the addition of AMT formed an adsorption film on the alloy surface, thus slowing down the corrosion process of aluminium alloy in NaCl solution.

Surface Characterization

To assess the surface morphology of AA2024 aluminium alloy exposed to the aggressive media, 3D profilometry and SEM images were performed on the alloy after immersion in 3.5 wt.% NaCl solution for 72 h without and with 1.5 g/L AMT inhibitor. It is clearly seen in **Figure 5** that the unprotected alloy surface was remarkably corroded with the appearance of many pits and corrosion products, and the surface roughness was as high as ~0.389 μm. On the contrary, the AMT protected aluminium surface was relative smooth and uniform, with a lower surface roughness value of 0.225 μm. It is known that the AA2024 alloy is highly susceptible to corrosion in NaCl solution due to the existence of IMPs, which have been demonstrated to be the active sites for localized corrosion (Zheludkevich et al., 2005). The EDX analysis from the red spot in **Figure 5A** revealed the presence of Al, Cu, Mg, Mn, C and O elements on the alloy surface, and the very high oxygen content verified the presence of corrosion products such as $Al(OH)_3$ and Al_2O_3 on the alloy matrix (Visser et al., 2019). For the AMT protected AA2024 surface, no corrosion pit was visible. The EDX results from the blue spot and the green spot in **Figure 5B** showed much lower oxygen content and higher Al content, demonstrating a low level of corrosion products on the alloy surface. Hence, the surface analysis data are in good agreement with the electrochemical data, indicating that AMT can considerably improve the corrosion resistance property of the aluminium alloy.

To investigate the hydrophilic and hydrophobic nature of different surfaces, the WCAs were tested on the AA2024 aluminium alloy after immersion in 3.5 wt.% NaCl solution for 72 h without and with 1.5 g/L AMT inhibitor. As shown in **Figure 6**, the blank alloy exhibited a WCA of 65.3°, and the inhibitor adsorbed alloy displayed a higher WCA of 76.8°. These results indicate that the corrosive media can reach the uninhibited alloy surface more easily, whereas there is a competitive adsorption between inhibitors and water molecules in solution on the AMT adsorbed surface. The increase of the adsorption ability of corrosion inhibitors strengthens the hydrophobicity of the metal surface, hence decreasing the corrosion tendency (Zhang et al., 2021).

Surface-Enhanced Raman Scattering Detection of Inhibitors

SERS technology is one of the most important surface analytical methods because of its rapid detection, high sensitivity, high selectivity, and *in-situ* characterization of the surface composition (Yue et al., 2022). The adsorption kinetics of AMT molecules on AA2024 alloy surfaces after different exposure time to NaCl solution was characterized by

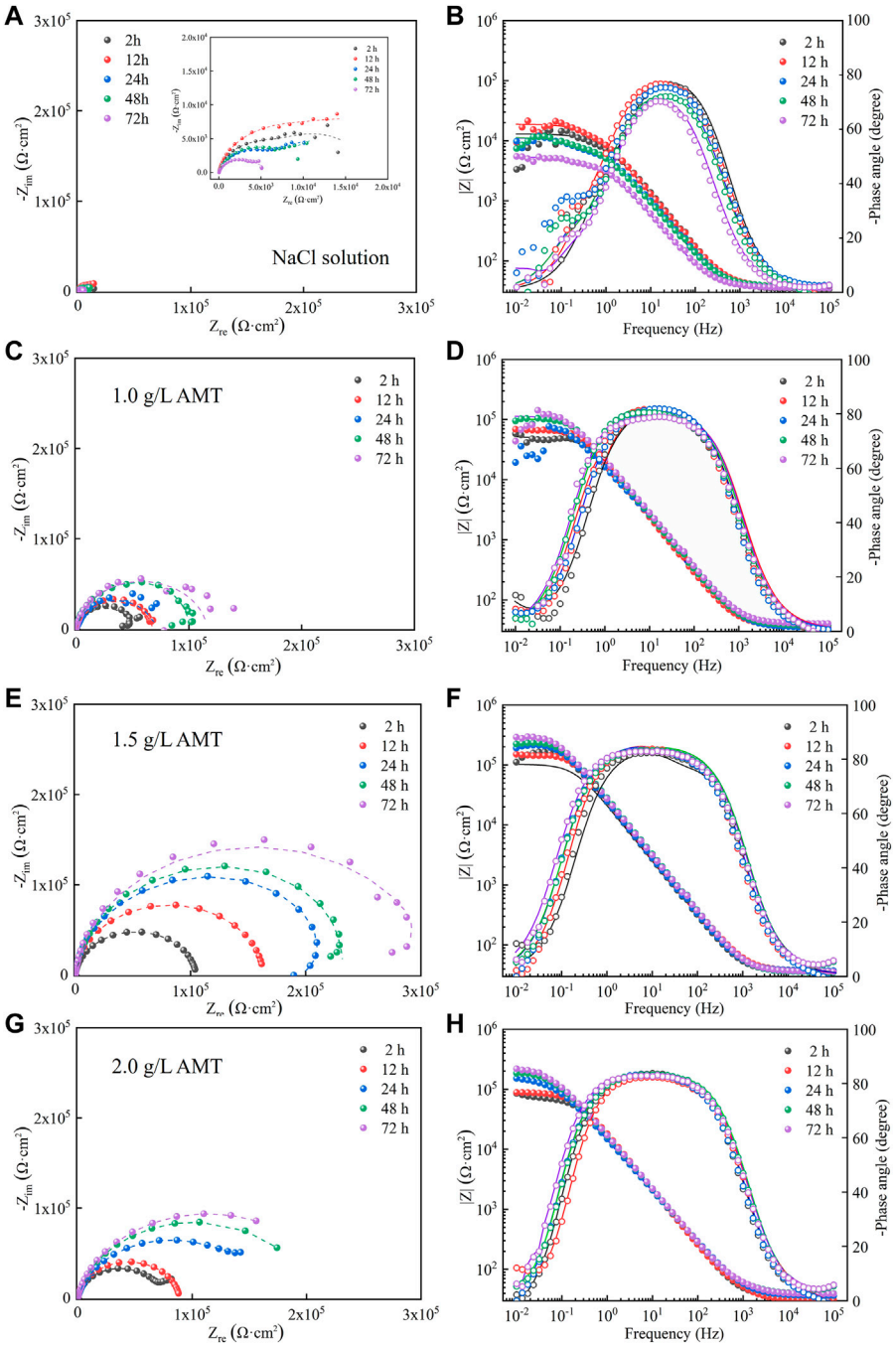

FIGURE 2 | (A,C,E,G) Nyquist diagrams and **(B,D,F,H)** Bode plots of AA2024 aluminium alloy in 3.5 wt.% NaCl solution containing different concentrations of AMT inhibitors.

SERS measurement, using silver nanorods decorated SERS active tape as the Raman signal amplifier (Wang et al., 2021; Ma et al., 2020). **Figure 7A** shows the SERS spectra of AMT molecules adsorbed on the surface of AA2024 aluminium alloy after immersing in 3.5 wt.% NaCl solution with 1.5 g/L AMT for different times. The SERS spectra clearly revealed the characteristic Raman bands of AMT molecules, including 702, 856, 929, 1,130, 1,405, and 1,606 cm^{-1}. The peaks at 702 and 929 cm^{-1} are attributed to triazole ring torsion. The peak at 856 cm^{-1} corresponds to the triazole ring breathing pattern. The peak value at 1,130 cm^{-1} is attributed to the N-N bending vibration. The peak at 1,405 cm^{-1} is assigned to the tensile vibration of the triazole ring. The peak at 1,606 cm^{-1} belongs to the bending vibration

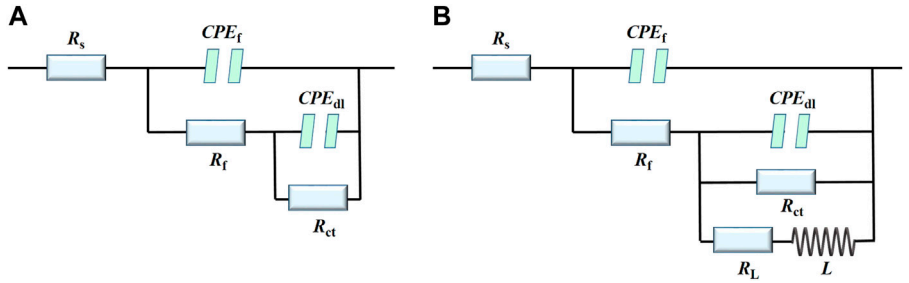

FIGURE 3 | EECs of AA2024 aluminium alloy in 3.5wt.% NaCl solution containing AMT.

TABLE 2 | EIS fitting data of AA2024 alloy in 3.5 wt.% NaCl solution containing different concentrations of AMT.

C_{AMT} (g/L)	Time (h)	Q_f ($\Omega^{-1}\cdot cm^{-2}\ S^n$)	n_f	R_f ($\Omega\cdot cm^2$)	Q_{dl} ($\Omega^{-1}\cdot cm^{-2}\cdot S^n$)	n_{dl}	R_{ct} ($\Omega\cdot cm^2$)	L (H cm^{-2})	R_L ($\Omega\cdot cm^2$)	χ^2 ($\times 10^{-3}$)
0	2	1.03×10^{-5}	0.93	9.37×10^{3}	7.70×10^{-5}	1.00	3.82×10^{3}	—	—	4.8
	12	1.27×10^{-5}	0.92	1.46×10^{4}	9.61×10^{-5}	1.00	4.62×10^{3}	—	—	2.0
	24	1.76×10^{-5}	0.89	7.40×10^{3}	2.77×10^{-4}	0.94	3.92×10^{3}	—	—	1.1
	48	1.52×10^{-5}	0.88	8.34×10^{3}	3.92×10^{-4}	1.00	3.16×10^{3}	—	—	1.1
	72	1.09×10^{-5}	0.90	6.97×10^{3}	4.32×10^{-4}	0.97	2.26×10^{3}	—	—	1.9
1.0	2	8.06×10^{-6}	0.94	5.14×10^{4}	3.87×10^{-5}	1.00	4.43×10^{4}	—	—	5.1
	12	8.29×10^{-6}	0.94	5.96×10^{4}	2.84×10^{-5}	1.00	5.03×10^{4}	—	—	1.5
	24	7.65×10^{-6}	0.90	6.94×10^{4}	6.40×10^{-6}	0.94	6.42×10^{4}	—	—	1.9
	48	7.21×10^{-6}	0.91	7.63×10^{4}	7.23×10^{-7}	1.00	7.83×10^{4}	1.83×10^{3}	3.03×10^{4}	1.6
	72	5.93×10^{-6}	0.92	8.71×10^{4}	7.72×10^{-7}	1.00	1.06×10^{5}	—	—	4.0
1.5	2	6.94×10^{-6}	0.94	7.34×10^{4}	8.22×10^{-7}	1.00	1.55×10^{5}	—	—	4.3
	12	6.21×10^{-6}	0.95	1.35×10^{5}	5.82×10^{-7}	1.00	2.11×10^{5}	—	—	1.7
	24	6.08×10^{-6}	0.94	1.95×10^{5}	5.42×10^{-7}	1.00	2.68×10^{5}	1.23×10^{4}	5.82×10^{4}	0.6
	48	4.26×10^{-6}	0.94	2.43×10^{5}	3.99×10^{-7}	0.98	3.07×10^{5}	3.10×10^{4}	8.24×10^{4}	0.6
	72	3.03×10^{-6}	0.94	2.62×10^{5}	1.30×10^{-7}	0.96	6.91×10^{5}	1.11×10^{5}	1.03×10^{5}	0.9
2.0	2	6.16×10^{-6}	0.93	4.49×10^{4}	9.66×10^{-7}	1.00	6.64×10^{4}	—	—	0.8
	12	6.21×10^{-6}	0.94	5.61×10^{4}	9.64×10^{-7}	0.88	8.88×10^{4}	—	—	5.1
	24	5.96×10^{-6}	0.87	7.97×10^{4}	6.84×10^{-7}	1.00	9.32×10^{4}	—	—	1.3
	48	5.12×10^{-6}	0.98	8.62×10^{4}	8.65×10^{-7}	1.00	2.06×10^{5}	—	—	3.2
	72	5.66×10^{-6}	0.88	1.25×10^{5}	7.97×10^{-7}	1.00	6.21×10^{5}	—	—	1.1

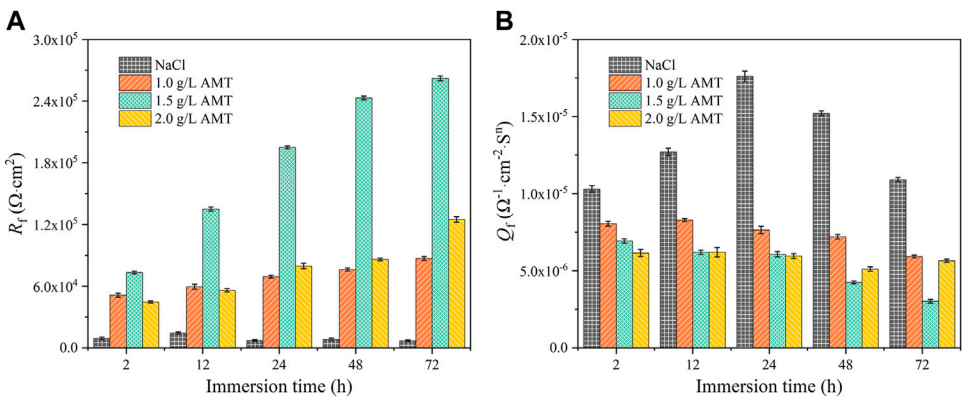

FIGURE 4 | Evaluation of **(A)** R_f and **(B)** Q_f parameters of AA2024 aluminium alloy in 3.5wt.% NaCl solution containing AMT.

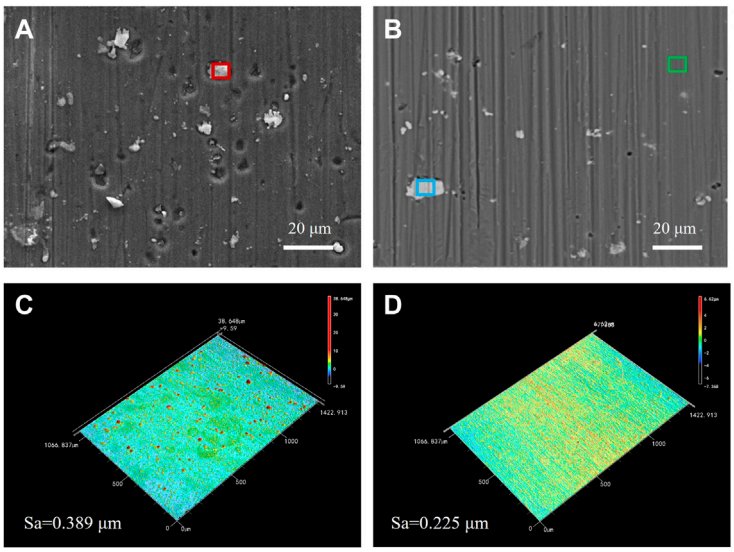

E

Element	Atomic percent (%)
C	17.66
O	14.89
Cu	8.10
Mg	1.48
Mn	0.46
Al	57.41

Element	Atomic percent (%)
C	15.22
O	6.22
Cu	17.31
Mg	1.00
Mn	0.10
Al	60.16

Element	Atomic percent (%)
C	10.62
O	3.82
Cu	1.33
Mg	2.52
Mn	0.31
Al	81.40

FIGURE 5 | SEM images after immersing the AA2024 aluminium alloy in 3.5 wt.% NaCl solution for 72 h **(A)** without and **(B)** with 1.5 g/L AMT inhibitors; CLSM images after immersing the AA2024 alloy in 3.5 wt.% NaCl solution for 72 h **(C)** without and **(D)** with 1.5 g/L AMT inhibitors; **(E)** EDX calculation results from the red, blue and green areas.

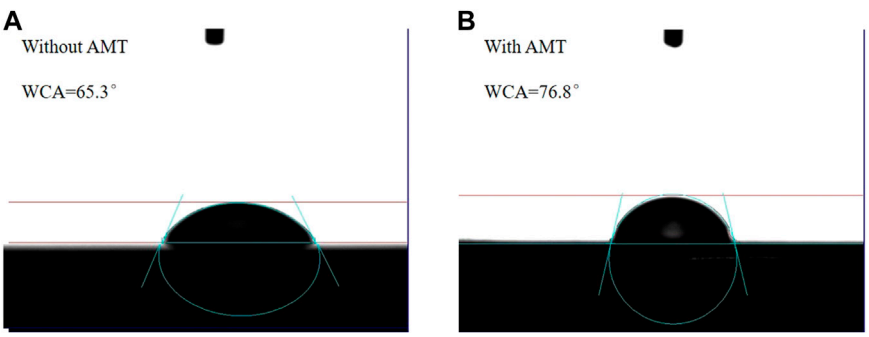

FIGURE 6 | The WCA of the AA2024 aluminium alloy after immersion in 3.5 wt.% NaCl solution for 72 h **(A)** without and **(B)** with 1.5 g/L AMT inhibitor.

of NH_2 (Sherif et al., 2010; Wang et al., 2011; Xavier and Gobinath, 2012). The appearance of these characteristic Raman peaks indicates that AMT molecules have been effectively adsorbed on the surface of AA2024 alloy. More importantly, the variation of Raman intensity can reflect the adsorption kinetics process of analytes. It is noted that with the increase of immersion time, the SERS signals on the aluminium alloy surface increased gradually. From 2 to 48 h, the SERS signals of corrosion inhibitors increased significantly, indicating that the adsorption rate was relatively high. Subsequently, the SERS intensity and corresponding adsorption amount reached saturation from 48 to 72 h. To correlate the AMT adsorption behavior with the corrosion inhibition property on the AA2024 alloy surface, **Figure 7B** plots the R_f values of the substrate immersed in 3.5 wt.% NaCl solution containing 1.5 g/L AMT versus the corresponding SERS peak intensities at 1,606 cm^{-1}. A positive correlation was clearly shown between the SERS signals and R_f values. Since the R_f parameter can reflect the surface coverage of inhibitor film, the dramatic increase of R_f value indicates the gradual coverage of metal surface via inhibitor adsorption, which is confirmed by the continuous increase and saturation of SERS signals during immersion.

XPS Characterization

To further identify the adsorption of corrosion inhibitors on the alloy surface, the chemical compositions of surface films were studied by XPS. **Figure 8** shows the XPS survey spectra and high resolution spectra of AA2024 aluminium alloy surface after immersion for 72 h in 3.5 wt.% NaCl solution without or with 1.5 g/L AMT inhibitors. It is seen that the peaks of Al, C and O elements were detected on the alloy

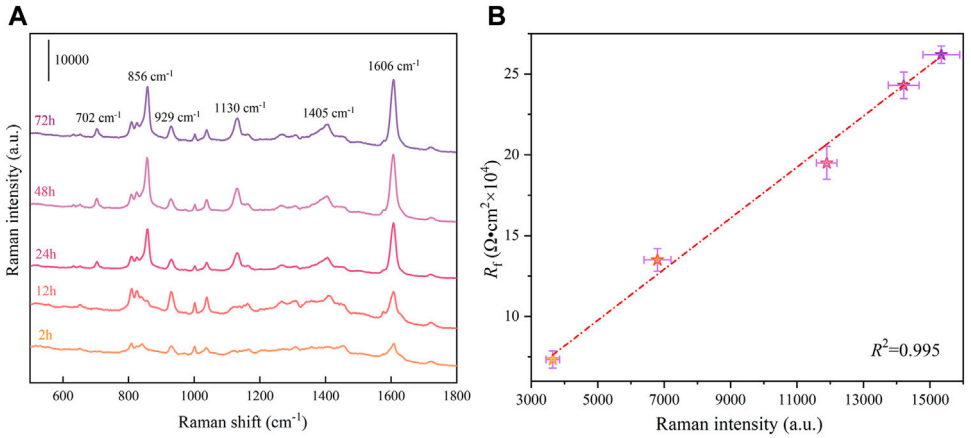

FIGURE 7 | (A) SERS spectra of AMT molecules adsorbed on the surface of AA2024 aluminium alloy after immersing in 3.5 wt.% NaCl solution with 1.5 g/L AMT for different times; **(B)** the R_f values of the substrate immersed in 3.5 wt.% NaCl solution containing 1.5 g/L AMT versus the corresponding SERS peak intensities at 1,606 cm^{-1}.

surface in blank solution. After adding inhibitors, new elemental peaks of S and N were shown, which were assigned to the AMT molecules. **Figure 8B** shows the high resolution peaks of Al 2p in the blank and inhibitor adsorbed alloy surfaces. The Al 2p spectrum consisted of three components at binding energies of 74.9, 74.3, and 73.1 eV, corresponding to $Al(OH)_3$, Al_2O_3 and AlO_x, respectively (Kozlica et al., 2021). **Figure 8C** illustrates the high resolution peaks of S 2p. The S element signal was not observed on the surface of blank AA2024 alloy. In the presence of AMT, the S 2p spectrum with two peaks was clearly seen. The peaks at 161.8 and 164.0 eV can be ascribed to

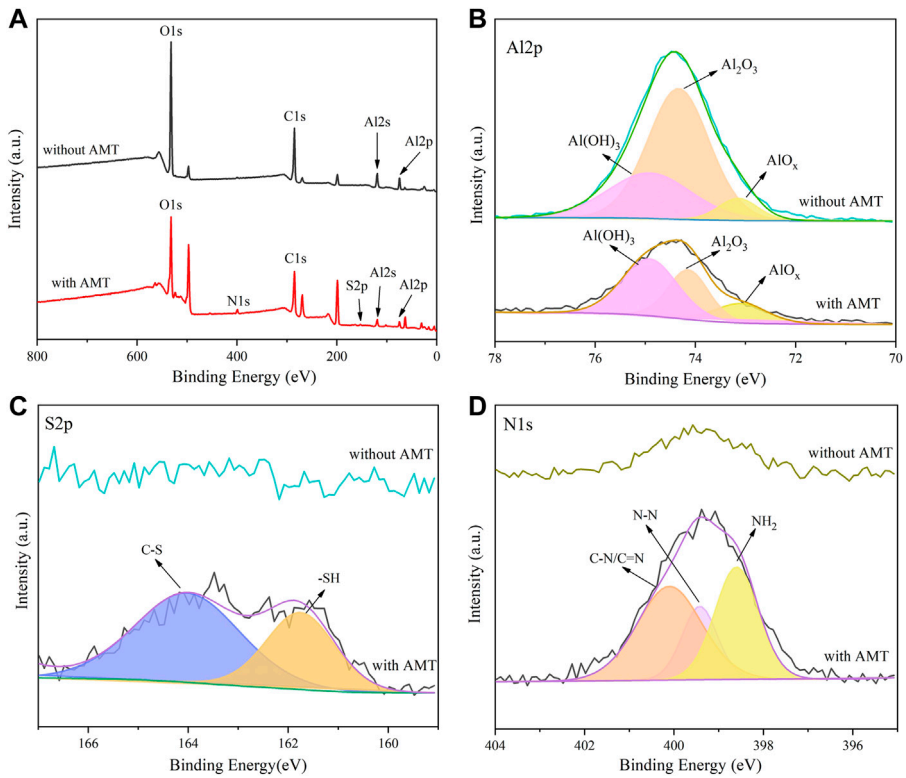

FIGURE 8 | The XPS survey spectra and high resolution spectra of AA2024 aluminium alloy surface after immersion for 72 h in 3.5 wt.% NaCl solution without or with 1.5 g/L AMT inhibitors.

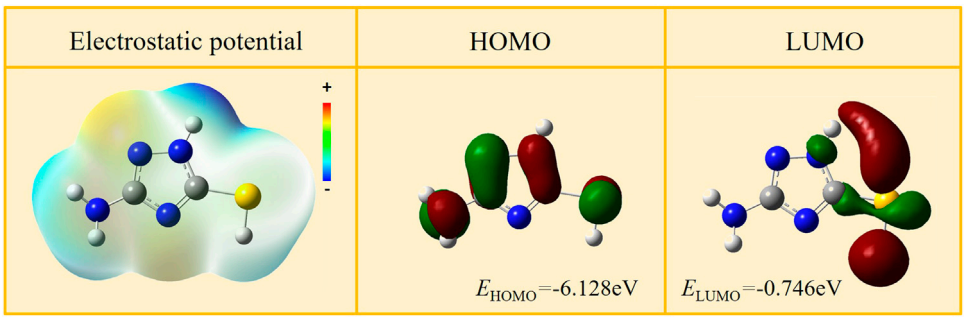

FIGURE 9 | Frontier molecular density distribution of the AMT molecule.

TABLE 3 | Fukui indices of AMT.

Atoms	f_-	f_+	f_0
C1	0.06	0.06	0.06
N2	0.05	0.05	0.05
N4	0.17	0.07	0.12
N5	0.08	0.04	0.07
C6	0.07	0.03	0.06
N7	0.16	0.03	0.10
S10	0.21	0.40	0.31

the sulfhydryl group and C-S bond between heterocycle and sulfhydryl group. As for the N 1s spectrum (**Figure 8D**), in the presence of AMT, it can be fitted into three peaks of 400.0, 399.4 and 398.6 eV, which were ascribed to the C-N/C=N, N-N and NH_2 bonds of AMT molecules (Huang and Bu, 2020). Therefore, the AMT inhibitors are successfully adsorbed on the alloy surface, which is in agreement with the results from EDS and Raman measurements.

Molecular Modeling

Quantum chemistry calculation of AMT molecules was carried out to further investigate the corrosion protection mechanism of AMT. **Figure 9** shows the highest occupied molecular orbital (HOMO) and the lowest unoccupied molecular orbital (LUMO) as well as the electrostatic potential (ESP) of AMT molecules. According to the Frontier molecular orbital theory, the transition of the electrons is mainly related to the HOMO and LUMO of a molecule (Pareek et al., 2019; Wang et al., 2022). As for AMT, the HOMO is distributed uniformly over the entire surface of the molecule, and the LUMO is localized around the S atom, which exhibits an extremely strong electron gaining ability as can be seen from the huge red region in the molecular orbital diagram.

We used condensed Fukui functions to analyze the local reactivity of molecules and quantitatively describe the possibility of each atom as an adsorption site. The sites with larger f values exhibit increased activity and are potential candidates to be adsorbed on metal surfaces (El-Hajjaji et al., 2020). **Table 3** shows the condensed Fukui functions and f values for the C, N, and S atoms of AMT molecules. **Figure 10** shows the corresponding graphs. As can be seen, N4 and N7 have large f_- values, which indicate that these atoms are preferred sites for electrons transfer from AMT molecules to metals during electrophilic attacks. S atom exhibits great electron-giving and electron-accepting ability owing to the much larger f_+ and f_- values, which is consistent

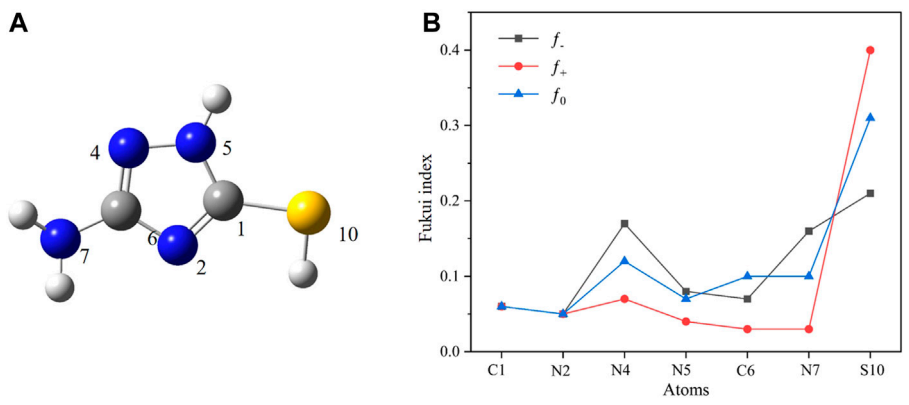

FIGURE 10 | (A) The optimized structure of AMT molecular; **(B)** Fukui indices and components of molecular orbitals of AMT.

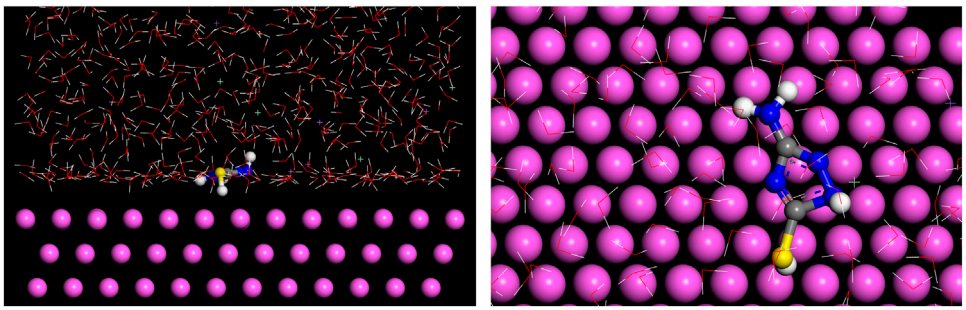

FIGURE 11 | Adsorption equilibrium configuration of AMT molecules on Al (111) surface.

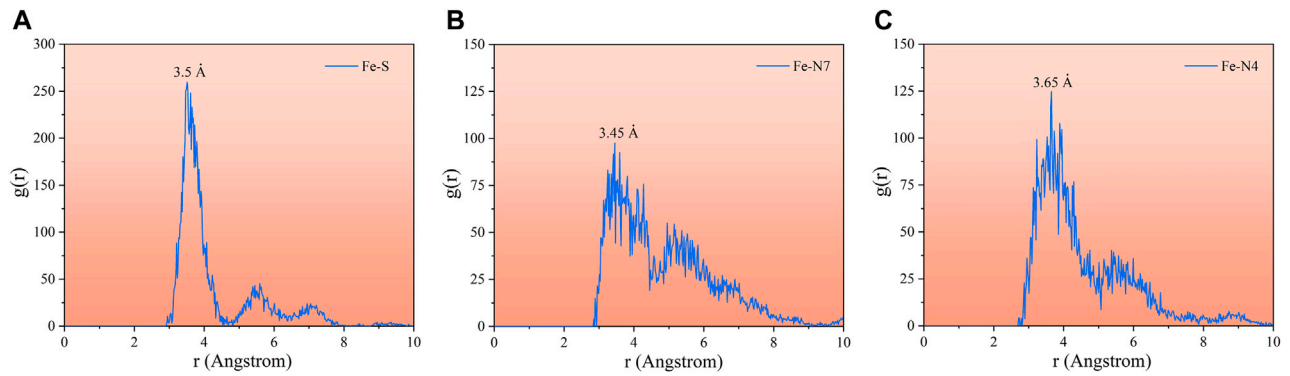

FIGURE 12 | The relevant RDF analysis of AMT molecule **(A)** Fe-S, **(B)** Fe-N7 and **(C)** Fe-N4.

with the conclusion of molecular orbital analysis. Therefore, special attention should be paid to these highly active sites when calculating the adsorption model of AMT molecule on metal surface.

Molecular dynamics simulation can provide novel insights into the interfacial interactions between organic molecules and metal substrates (Kovačević and Kokalj, 2011). **Figure 11** shows the side and the top views of the equilibrium adsorption configuration of AMT molecule on Al (111) surface. AMT adsorbs on the Al surface in a nearby flat manner, which is beneficial for improving the surface coverage of AMT on the metal surface (Bouoidina et al., 2021). The electron-giving and electron-receiving processes of AMT adsorption are promoted by S and N atoms (Luo et al., 2021). These interactions lead to the formation of coordination bonds between AMT and Al surface, and can form a compact film that prevents the aggressive media to reach the metal surface (Ammouchi et al., 2020; Li et al., 2022).

The radial distribution function (RDF) g (r) derived from MD orbital data is a good method to estimate the bond information. Generally, peak bond lengths from 1 to 3.5 Å are associated with the chemisorption, while those beyond 3.5 Å are assigned to the physical interactions (Lgaz et al., 2017; Singh et al., 2018). **Figure 12** shows the RDF analysis of the major heteroatoms of the AMT molecule on the Al (111) surface. As can be seen from the figure, the bond lengths of Fe-N7 (3.45 Å) and Fe-S (3.5 Å) are no more than 3.5 Å, which means that the N7 and S atoms are attached to the metal substrate via chemisorption; on the other hand, N4 (3.65 Å) is adsorbed on the metal substrate as physical adsorption. These findings confirm that these active centers have great ability for donating and accepting electrons to/from Al that lead to good inhibition performance of the studied AMT molecules.

CONCLUSION

In this work, the excellent corrosion inhibition effect of AMT on AA2024 aluminium alloy in 3.5 wt.% NaCl solution was demonstrated by electrochemical test and surface analysis, and the corrosion inhibition mechanism was explained by DFT and molecular dynamics simulation. AMT mainly acted as a cathode-type corrosion inhibitor, and the highest corrosion inhibition efficiency was achieved when the concentration of AMT was

1.5 g/L. SERS spectra characterized the adsorption kinetics process of AMT on the alloy surface, and a positive correlation between the SERS signals and R_f values was clearly shown, which indicated that the continuous adsorption of AMT strengthened the corrosion inhibition efficiency. The heterogeneous donor atoms (N and S) of AMT molecule can act as the active sites to contribute to the bonding of the metal surface. The adsorbed AMT molecules tended to adsorb on the Al (111) surface in the parallel orientation to obtain the maximum coverage.

DATA AVAILABILITY STATEMENT

The raw data supporting the conclusion of this article will be made available by the authors, without undue reservation.

AUTHOR CONTRIBUTIONS

XG: Conceptualization, methodology, software. JW: Data curation, writing—original draft preparation. LH: Visualization. YW: Investigation. LM: Supervision. DZ: Supervision, validation. LWM: Writing—reviewing and editing.

FUNDING

This work was supported by the National Natural Science Foundation of China (No. 51901015); Young Elite Scientists Sponsorship Program by China Association for Science and Technology (YESS, 2020QNRC001); and the Research Fund of State Key Laboratory for Marine Corrosion and Protection, Luoyang Ship Material Research Institute (LSMRI) under the contract No. KFJS1902.

REFERENCES

Abdallah, M. (2004). Antibacterial Drugs as Corrosion Inhibitors for Corrosion of Aluminium in Hydrochloric Solution. *Corrosion Sci.* 46, 1981–1996. doi:10.1016/j.corsci.2003.09.031

Al Zoubi, W., and Ko, Y. G. (2019). Self-assembly of Hierarchical N-Heterocycles-Inorganic Materials into Three-Dimensional Structure for superior Corrosion protection. *Chem. Eng. J.* 356, 850–856. doi:10.1016/j.cej.2018.09.089

Ammouchi, N., Allal, H., Belhocine, Y., Bettaz, S., and Zouaoui, E. (2020). DFT Computations and Molecular Dynamics Investigations on Conformers of Some Pyrazinamide Derivatives as Corrosion Inhibitors for Aluminum. *J. Mol. Liquids* 300, 112309. doi:10.1016/j.molliq.2019.112309

Balbo, A., Chiavari, C., Martini, C., and Monticelli, C. (2012). Effectiveness of Corrosion Inhibitor Films for the Conservation of Bronzes and Gilded Bronzes. *Corrosion Sci.* 59, 204–212. doi:10.1016/j.corsci.2012.03.003

Bouoidina, A., Ech-chihbi, E., El-Hajjaji, F., El Ibrahimi, B., Kaya, S., and Taleb, M. (2021). Anisole Derivatives as Sustainable-green Inhibitors for Mild Steel Corrosion in 1 M HCl: DFT and Molecular Dynamic Simulations Approach. *J. Mol. Liquids* 324, 115088. doi:10.1016/j.molliq.2018.08.05310.1016/j.molliq.2020.115088

Cao, K., Huang, W., Huang, X., and Pan, J. (2022). Imidazo [1,2-a] Pyrimidine Derivatives as Effective Inhibitor of Mild Steel Corrosion in HCl Solution: Experimental and Theoretical Studies. *Front. Mater.* 9, 843522. doi:10.3389/fmats.2022.843522

Coelho, L. B., Cossement, D., and Olivier, M.-G. (2018). Benzotriazole and Cerium Chloride as Corrosion Inhibitors for AA2024-T3: An EIS Investigation Supported by SVET and ToF-SIMS Analysis. *Corrosion Sci.* 130, 177–189. doi:10.1016/j.corsci.2017.11.004

Dutta, A., Saha, S. K., Adhikari, U., Banerjee, P., and Sukul, D. (2017). Effect of Substitution on Corrosion Inhibition Properties of 2-(substituted Phenyl) Benzimidazole Derivatives on Mild Steel in 1 M HCl Solution: a Combined Experimental and Theoretical Approach. *Corrosion Sci.* 123, 256–266. doi:10.1016/j.corsci.2017.04.017

El-Hajjaji, F., Ech-Chihbi, E., Rezki, N., Benhiba, F., Taleb, M., Chauhan, D. S., et al. (2020). Electrochemical and Theoretical Insights on the Adsorption and Corrosion Inhibition of Novel Pyridinium-Derived Ionic Liquids for Mild Steel in 1 M HCl. *J. Mol. Liquids* 314, 113737. doi:10.1016/j.molliq.2020.113737

El-Naggar, M. M. (2007). Corrosion Inhibition of Mild Steel in Acidic Medium by Some Sulfa Drugs Compounds. *Corrosion Sci.* 49, 2226–2236. doi:10.1016/j.corsci.2006.10.039

Fekry, A. M., Ghoneim, A. A., and Ameer, M. A. (2014). Electrochemical Impedance Spectroscopy of Chitosan Coated Magnesium Alloys in a Synthetic Sweat Medium. *Surf. Coat. Tech.* 238, 126–132. doi:10.1016/j.surfcoat.2013.10.058

Hao, Y., Sani, L. A., Ge, T., and Fang, Q. (2017). The Synergistic Inhibition Behaviour of Tannic Acid and Iodide Ions on Mild Steel in H 2 SO 4 Solutions. *Corrosion Sci.* 123, 158–169. doi:10.1016/j.corsci.2017.05.001

Hashimoto, T., Zhang, X., Zhou, X., Skeldon, P., Haigh, S. J., and Thompson, G. E. (2016). Investigation of Dealloying of S Phase (Al 2 CuMg) in AA 2024-T3 Aluminium alloy Using High Resolution 2D and 3D Electron Imaging. *Corrosion Sci.* 103, 157–164. doi:10.1016/j.corsci.2015.11.013

Huang, H., and Bu, F. (2020). Correlations between the Inhibition Performances and the Inhibitor Structures of Some Azoles on the Galvanic Corrosion of Copper Coupled with Silver in Artificial Seawater. *Corrosion Sci.* 165, 108413. doi:10.1016/j.corsci.2019.108413

Kovačević, N., and Kokalj, A. (2011). Analysis of Molecular Electronic Structure of Imidazole- and Benzimidazole-Based Inhibitors: A Simple Recipe for Qualitative Estimation of Chemical Hardness. *Corrosion Sci.* 53, 909–921. doi:10.1016/j.corsci.2010.11.016

Kozlica, D. K., Kokalj, A., and Milošev, I. (2021). Synergistic Effect of 2-mercaptobenzimidazole and Octylphosphonic Acid as Corrosion Inhibitors for Copper and Aluminium - an Electrochemical, XPS, FTIR and DFT Study. *Corrosion Sci.* 182, 109082. doi:10.1016/j.corsci.2020.109082

Lgaz, H., Salghi, R., Subrahmanya Bhat, K., Chaouiki, A., Shubhalaxmiand Jodeh, S. (2017). Correlated Experimental and Theoretical Study on Inhibition Behavior of Novel Quinoline Derivatives for the Corrosion of Mild Steel in Hydrochloric Acid Solution. *J. Mol. Liquids* 244, 154–168. doi:10.1016/j.molliq.2017.08.121

Li, Q., Xia, X., Pei, Z., Cheng, X., Zhang, D., Xiao, K., et al. (2022). Long-term Corrosion Monitoring of Carbon Steels and Environmental Correlation Analysis via the Random forest Method. *Npj Mater. Degrad.* 6, 1. doi:10.1038/s41529-021-00211-3

Liao, L. L., Mo, S., Luo, H. Q., and Li, N. B. (2017). Longan Seed and Peel as Environmentally Friendly Corrosion Inhibitor for Mild Steel in Acid Solution: Experimental and Theoretical Studies. *J. Colloid Interf. Sci.* 499, 110–119. doi:10.1016/j.jcis.2017.03.091

Liu, J., Wang, D., Gao, L., and Zhang, D. (2016). Synergism between Cerium Nitrate and Sodium Dodecylbenzenesulfonate on Corrosion of AA5052 Aluminium alloy in 3 wt.% NaCl Solution. *Appl. Surf. Sci.* 389, 369–377. doi:10.1016/j.apsusc.2016.07.107

Luo, X., Dong, C., Xi, Y., Ren, C., Wu, J., Zhang, D., et al. (2021). Computational Simulation and Efficient Evaluation on Corrosion Inhibitors for Electrochemical Etching on Aluminum Foil. *Corrosion Sci.* 187, 109492. doi:10.1016/j.corsci.2021.109492

Ma, L., Wang, J., Ren, C., Ju, P., Huang, Y., Zhang, F., et al. (2020). Detection of Corrosion Inhibitor Adsorption via a Surface-Enhanced Raman Spectroscopy (SERS) Silver Nanorods Tape Sensor. *Sensors Actuators B: Chem.* 321, 128617. doi:10.1016/j.snb.2020.128617

Ma, L., Wang, J., Zhang, D., Huang, Y., Huang, L., Wang, P., et al. (2021). Dual-action Self-Healing Protective Coatings with Photothermal Responsive Corrosion Inhibitor Nanocontainers. *Chem. Eng. J.* 404, 127118. doi:10.1016/j.cej.2020.127118

Marcelin, S., and Pébère, N. (2015). Synergistic Effect between 8-hydroxyquinoline and Benzotriazole for the Corrosion protection of 2024 Aluminium alloy: a

Local Electrochemical Impedance Approach. *Corrosion Sci.* 101, 66–74. doi:10.1016/j.corsci.2015.09.002

Obot, I. B., Obi-Egbedi, N. O., and Umoren, S. A. (2009). Antifungal Drugs as Corrosion Inhibitors for Aluminium in 0.1M HCl. *Corrosion Sci.* 51, 1868–1875. doi:10.1016/j.corsci.2009.05.017

Pareek, H., Jain, D., Hussain, S., Biswas, A., Shrivastava, R., Parida, S. K., et al. (2019). A New Insight into Corrosion Inhibition Mechanism of Copper in Aerated 3.5 wt.% NaCl Solution by Eco-Friendly Imidazopyrimidine Dye: Experimental and Theoretical Approach. *Chem. Eng. J.* 358, 725–742. doi:10.1016/j.cej.2018.08.079

Parvizi, R., Hughes, A. E., Glenn, A. M., Cizek, P., Tan, M. Y., and Forsyth, M. (2018). Role of Microstructure in Corrosion Initiation of a Highly-Deformed AA2024 Wire. *Corrosion Sci.* 144, 184–197. doi:10.1016/j.corsci.2018.08.052

Qiang, Y., Zhang, S., Xu, S., and Li, W. (2016). Experimental and Theoretical Studies on the Corrosion Inhibition of Copper by Two Indazole Derivatives in 3.0% NaCl Solution. *J. Colloid Interf. Sci.* 472, 52–59. doi:10.1016/j.jcis.2016.03.023

Recloux, I., Andreatta, F., Druart, M.-E., Coelho, L. B., Cepek, C., Cossement, D., et al. (2018). Stability of Benzotriazole-Based Films against AA2024 Aluminium alloy Corrosion Process in Neutral Chloride Electrolyte. *J. Alloys Comp.* 735, 2512–2522. doi:10.1016/j.jallcom.2017.11.346

Shen, S., Guo, X.-y., Song, P., Pan, Y.-C., Wang, H.-q., Wen, Y., et al. (2013). Phytic Acid Adsorption on the Copper Surface: Observation of Electrochemistry and Raman Spectroscopy. *Appl. Surf. Sci.* 276, 167–173. doi:10.1016/j.apsusc.2013.03.061

Sherif, E.-S. M., Erasmus, R. M., and Comins, J. D. (2010). *In Situ* Raman Spectroscopy and Electrochemical Techniques for Studying Corrosion and Corrosion Inhibition of Iron in Sodium Chloride Solutions. *Electrochimica Acta* 55, 3657–3663. doi:10.1016/j.electacta.2010.01.117

Sherif, E. M., and Park, S. M. (2006). 2-Amino-5-ethyl-1, 3, 4-thiadiazole as a Corrosion Inhibitor for Copper in 3.0% NaCl Solutions. *Corros. Sci.* 48, 4065–4079. doi:10.1016/j.corsci.2006.03.011

Singh, A., Ansari, K. R., Haque, J., Dohare, P., Lgaz, H., Salghi, R., et al. (2018). Effect of Electron Donating Functional Groups on Corrosion Inhibition of Mild Steel in Hydrochloric Acid: Experimental and Quantum Chemical Study. *J. Taiwan Inst. Chem. Eng.* 82, 233–251. doi:10.1016/j.jtice.2017.09.021

Visser, P., Marcoen, K., Trindade, G. F., Abel, M.-L., Watts, J. F., Hauffman, T., et al. (2019). The Chemical Throwing Power of Lithium-Based Inhibitors from Organic Coatings on AA2024-T3. *Corrosion Sci.* 150, 194–206. doi:10.1016/j.corsci.2019.02.009

Wang, J., Ma, L., Guo, X., Wu, S., Liu, T., Yang, J., et al. (2022). Two Birds with One Stone: Nanocontainers with Synergetic Inhibition and Corrosion Sensing Abilities towards Intelligent Self-Healing and Self-Reporting Coating. *Chem. Eng. J.* 433, 134515. doi:10.1016/j.cej.2022.134515

Wang, X., Liu, X., and Wang, X. (2011). Self-assembled Synthesis of Ag Nanodendrites and Their Applications to SERS. *J. Mol. Struct.* 997, 64–69. doi:10.1016/j.molstruc.2011.04.041

Wang, Y., Wang, J., Ma, L., Ren, C., Zhang, D., Ma, L., et al. (2021). Qualitative and Quantitative Detection of Corrosion Inhibitors Using Surface-Enhanced Raman Scattering Coupled with Multivariate Analysis. *Appl. Surf. Sci.* 568, 150967. doi:10.1016/j.apsusc.2021.150967

Wang, Z., Chen, P., Li, H., Fang, B., Song, R., and Zheng, Z. (2017). The Intergranular Corrosion Susceptibility of 2024 Al alloy during Re-ageing after Solution Treating and Cold-Rolling. *Corrosion Sci.* 114, 156–168. doi:10.1016/j.corsci.2016.11.013

Wang, Z., Gong, Y., Zhang, L., Jing, C., Gao, F., Zhang, S., et al. (2018). Self-assembly of New Dendrimers Basing on strong π-π Intermolecular Interaction for Application to Protect Copper. *Chem. Eng. J.* 342, 238–250. doi:10.1016/j.cej.2018.02.080

Xavier, R. J., and Gobinath, E. (2012). FT-IR, FT-Raman, Ab Initio and DFT Studies, HOMO-LUMO and NBO Analysis of 3-Amino-5-Mercapto-1,2,4-Triazole. *Spectrochimica Acta A: Mol. Biomol. Spectrosc.* 86, 242–251. doi:10.1016/j.saa.2011.10.031

Yan, T., Zhang, S., Feng, L., Qiang, Y., Lu, L., Fu, D., et al. (2020). Investigation of Imidazole Derivatives as Corrosion Inhibitors of Copper in Sulfuric Acid: Combination of Experimental and Theoretical Researches. *J. Taiwan Inst. Chem. Eng.* 106, 118–129. doi:10.1016/j.jtice.2019.10.014

Yu, J., Li, J., and Gan, F. (2010). Inhibition of Copper Corrosion in Deionized Water by 3-Amino-5-Mercapto-1, 2, 4-triazole. *J. Chin. Soc. Corrosion Prot.* 30, 21–24.

Yue, S., Fang, J., and Xu, Z. (2022). Advances in Droplet Microfluidics for SERS and Raman Analysis. *Biosens. Bioelectron.* 198, 113822. doi:10.1016/j.bios.2021.113822

Zeng, Y., Kang, L., Wu, Y., Wan, S., Liao, B., Li, N., et al. (2021). Melamine Modified Carbon Dots as High Effective Corrosion Inhibitor for Q235 Carbon Steel in Neutral 3.5 Wt% NaCl Solution. *J. Mol. Liq.* 349, 118108. doi:10.1016/j.molliq.2021.118108

Zhang, R., Xiong, L., He, Z., Pu, J., and Guo, L. (2021). Synthesis and Structure of Water-Soluble Sb Quantum Dots and Enhanced Corrosion Inhibition Performance and Mechanisms. *Inorg. Chem.* 60, 16346–16356. doi:10.1021/acs.inorgchem.1c02172

Zhang, X., Pan, G., Hu, L., and Wang, H. C. (2020). Effects of Nitrilotriacetic Acid and Corrosion Inhibitor on Cobalt Barrier Chemical-Mechanical Polishing: Experimental and Density Functional Theory Analysis. *Colloids Surf. A: Physicochemical Eng. Aspects* 605, 125392. doi:10.1016/j.colsurfa.2020.125392

Zheludkevich, M. L., Yasakau, K. A., Poznyak, S. K., and Ferreira, M. G. S. (2005). Triazole and Thiazole Derivatives as Corrosion Inhibitors for AA2024 Aluminium alloy. *Corrosion Sci.* 47, 3368–3383. doi:10.1016/j.corsci.2005.05.040

Zhu, M., He, Z., Guo, L., Zhang, R., Anadebe, V. C., Obot, I. B., et al. (2021). Corrosion Inhibition of Eco-Friendly Nitrogen-Doped Carbon Dots for Carbon Steel in Acidic media: Performance and Mechanism Investigation. *J. Mol. Liquids* 342, 117583. doi:10.1016/j.molliq.2021.117583

Conflict of Interest: All authors declare that the research was conducted in the absence of any commercial or financial relationships that could be construed as a potential conflict of interest.